

2014-05

Evaluation of disconnected quark loops for hadron structure using GPUs

Alexandrou, C

<http://hdl.handle.net/10026.1/11017>

10.1016/j.cpc.2014.01.009

Computer Physics Communications

Elsevier BV

All content in PEARL is protected by copyright law. Author manuscripts are made available in accordance with publisher policies. Please cite only the published version using the details provided on the item record or document. In the absence of an open licence (e.g. Creative Commons), permissions for further reuse of content should be sought from the publisher or author.

Evaluation of disconnected quark loops for hadron structure using GPUs

C. Alexandrou ^{(a,b)*}, M. Constantinou ^(a), V. Drach ^(c), K. Hadjiyiannakou ^(a),
 K. Jansen ^(a,c), G. Koutsou ^(b), A. Strelchenko ^{(b)†}, A. Vaquero ^(b)
^(a) *Department of Physics, University of Cyprus, P.O. Box 20537, 1678 Nicosia, Cyprus*
^(b) *Computation-based Science and Technology Research Center,
 The Cyprus Institute, 20 Kavafi Str., Nicosia 2121, Cyprus*
^(c) *NIC, DESY, Platanenallee 6, D-15738 Zeuthen, Germany*
 (Dated: February 5, 2014)

A number of stochastic methods developed for the calculation of fermion loops are investigated and compared, in particular with respect to their efficiency when implemented on Graphics Processing Units (GPUs). We assess the performance of the various methods by studying the convergence and statistical accuracy obtained for observables that require a large number of stochastic noise vectors, such as the isoscalar nucleon axial charge. The various methods are also examined for the evaluation of sigma-terms where noise reduction techniques specific to the twisted mass formulation can be utilized thus reducing the required number of stochastic noise vectors.

PACS numbers: 11.15.Ha, 12.38.Gc, 12.38.Aw, 12.38.-t, 14.70.Dj

I. INTRODUCTION

The evaluation of disconnected quark loops is of paramount importance in order to eliminate a systematic error inherent in the determination of hadron matrix elements in lattice QCD. For flavor singlet quantities, these contributions, even though smaller in magnitude as compared to the connected contributions that are computationally easier to evaluate, are substantial and cannot be neglected. The explanation of why these quark loop contributions are large for flavor singlet quantities is the fact that, in a flavor singlet, the disconnected contributions coming from different flavors add up, and hence there is no *a priori* reason to neglect them. Naive perturbative calculations of some of these flavor singlet contributions differ from their experimental value, which suggests that flavor singlet phenomena are inherently linked with non-perturbative properties of the vacuum. A good example to support this point is the axial anomaly in the case of the η' mass, which is connected to the topological properties and non-perturbative nature of QCD.

The computation of disconnected quark loops within the lattice QCD formulation requires the calculation of all-to-all or time-slice-to-all propagators, which are impractical to compute exactly, and for which the computational resources required to estimate them with, e.g. stochastic methods, are much larger than those required for the corresponding connected contributions. Therefore, in most hadron studies up to now the disconnected contributions were neglected introducing an uncontrolled systematic uncertainty.

Recent progress in algorithms, however, combined with the increase in computational power, have made such cal-

culations feasible. On the algorithmic side, a number of improvements like the one-end trick [1–3], dilution [4–8], the Truncated Solver Method (TSM) [8–10] and the Hopping Parameter Expansion (HPE) [1, 11] have led to a significant reduction in both stochastic and gauge noise associated with the evaluation of disconnected quark loops. Moreover, using special properties of the twisted mass fermion Lagrangian, one can further enhance the signal-to-noise ratio by taking the appropriate combination of flavors. On the hardware side, graphics cards (GPUs) can provide a large speed-up in the evaluation of quark propagators and contractions. In particular, for the TSM, which relies on a large number of inversions of the Dirac matrix in single or half precision, GPUs provide an optimal platform.

In this paper, our aim is to assess recently developed methods and examine how reliably one can compute disconnected contributions to flavor singlet quantities by combining the algorithmic advances with the numerical power of GPUs. We will describe the various improvements using one ensemble of twisted mass fermion (TMF) gauge field configurations. The ensemble is generated with two light degenerate quarks and a strange and charm quark with masses fixed to their physical values, referred to as $N_f = 2 + 1 + 1$ simulations. The lattice size is $32^3 \times 64$, the lattice spacing extracted from the nucleon mass [12] $a = 0.082(1)(4)$ and pion mass about 370 MeV. This ensemble will be hereafter referred to as the B55.32 ensemble. This paper intends to describe the methodology and identify the efficiency of the various methods with respect to the observable under investigation, rather than to arrive at precise physical results. The latter we reserve for a follow-up publication. Although we will use the nucleon to test our methodology the conclusions apply to any hadron. The paper is organized as follows: in Section II we present the algorithms and variance reduction techniques we will employ. In Section III we explain our particular formulation, including information on the gauge configurations used, as well as details on the GPU

*email:alexand@ucy.ac.cy

†Present address: Scientific Computing Division, Fermilab, Batavia, IL 60510-5011, USA

implementation of our methods. Section IV explains our analysis to extract the desired matrix elements, followed by Section V in which we summarize the comparisons between the different methods employed. In Section VI we give our conclusions and outlook.

II. METHODS FOR DISCONNECTED CALCULATIONS

A. Stochastic estimate

The exact computation of all-to-all (time-slice-to-all) propagators on a lattice volume of physical interest is outside our current computer power, since this would require volume (spatial volume) times inversions of the Dirac matrix, whose size ranges from $\sim 10^7$ for a $24^3 \times 48$ lattice to $\sim 10^9$ for the largest volumes of $96^3 \times 192$ considered nowadays. The typical way around this problem is to compute an unbiased stochastic estimate of the all-to-all propagator [13]. The method consists of generating a set of N_r sources $|\eta_r\rangle$ randomly, by filling each component of the source with random numbers drawn from a particular representation of the \mathbb{Z}_2 or \mathbb{Z}_4 groups (more exactly $\{1, -1\}$ for \mathbb{Z}_2 and $\{1, i, -1, -i\}$ for \mathbb{Z}_4), or from a representation of $\mathbb{Z}_2 \otimes i\mathbb{Z}_2$. Other noise sets may be used, however it has been shown that \mathbb{Z}_N -noise has smaller variance than e.g. gaussian noise [14]. The \mathbb{Z}_N -noise sources have the following properties:

$$\frac{1}{N_r} \sum_{r=1}^{N_r} |\eta_r\rangle = |0\rangle + \mathcal{O}\left(\frac{1}{\sqrt{N_r}}\right), \quad (1)$$

$$\frac{1}{N_r} \sum_{r=1}^{N_r} |\eta_r\rangle \langle \eta_r| = \mathbb{I} + \mathcal{O}\left(\frac{1}{\sqrt{N_r}}\right). \quad (2)$$

The first property ensures that our estimate of the propagator is unbiased. The second one allows us to reconstruct the inverse matrix by solving for $|s_r\rangle$ in

$$M |s_r\rangle = |\eta_r\rangle \quad (3)$$

and calculating

$$M_E^{-1} := \frac{1}{N_r} \sum_{r=1}^{N_r} |s_r\rangle \langle \eta_r| \approx M^{-1}. \quad (4)$$

Since in general the number of noise vectors N_r required is much smaller than the lattice volume V , the computation becomes feasible, although it can still be very expensive depending on the value of N_r required to achieve a good estimate of M^{-1} in Eq. (4).

The deviation of our estimator from the exact solution is given by

$$M^{-1} - M_E^{-1} = M^{-1} \times \left(\mathbb{I} - \frac{1}{N_r} \sum_{r=1}^{N_r} |\eta\rangle \langle \eta| \right), \quad (5)$$

so as N_r increases the introduced stochastic error decreases, as Eq. (2) clearly shows. In fact, from Eqs. (2), (5) we see that the errors decrease as $\mathcal{O}\left(\frac{1}{\sqrt{N_r}}\right)$, as expected from the properties of these noise sources.

Since we have to deal with gauge error, i.e. the error coming from the fact that we analyze a representative set of gauge configurations, the number of stochastic noise sources should be taken so that the stochastic error is comparable to the gauge error. This criterion ideally determines the number of stochastic sources N_r , which can differ for each observable. Since we will be interested in evaluating a range of observables we will choose N_r that can yield good results for the most demanding among these observables.

B. The Truncated Solver Method

The Truncated Solver Method (TSM) [8–10] is a way to increase N_r at a reduced computational cost. The idea behind the method is the following: instead of inverting to high precision the stochastic sources in Eq. (3), we can aim at a low precision (LP) estimate

$$|s_r\rangle_{LP} = (M^{-1})_{LP} |\eta_r\rangle, \quad (6)$$

where the inverter, which is a Conjugate Gradient (CG) solver in this work, is truncated. The truncation criterion can be a low precision stop condition for the residual (for instance, $|\hat{r}| < 10^{-2}$, with \hat{r} the residual vector in the CG algorithm), or a fixed number of iterations, roughly around 1/10 or 1/20 of what would be needed to obtain a high precision (HP) solution. This way we can increase the number of stochastic sources N_{LP} at a very small cost. Using the low precision sources our estimate of the inverse matrix given by Eq. (4) is not unbiased, so we are introducing new errors in the computation of the all-to-all propagator.

In order to correct for the bias introduced using low precision, we estimate the correction C_E to this bias stochastically by inverting a number of sources to high and low precision, and calculating the difference,

$$C_E := \frac{1}{N_{HP}} \sum_{r=1}^{N_{HP}} [|s_r\rangle_{HP} - |s_r\rangle_{LP}] \langle \eta_r|, \quad (7)$$

where the $|s_r\rangle_{HP}$ are calculated by solving Eq. (3) up to high precision, so our final estimate becomes

$$M_{E_{TSM}}^{-1} := \frac{1}{N_{HP}} \sum_{r=1}^{N_{HP}} [|s_r\rangle_{HP} - |s_r\rangle_{LP}] \langle \eta_r| + \frac{1}{N_{LP}} \sum_{j=N_{HP}+1}^{N_{HP}+N_{LP}} |s_r\rangle_{LP} \langle \eta_r|, \quad (8)$$

which requires N_{HP} high precision inversions and $N_{HP} + N_{LP}$ low precision inversions. Following the discussion in

Ref. [15], one expects the error of this improved estimate of the fermion loop to scale as:

$$e\sqrt{2(1-r_c)+\frac{1}{n_{\text{LP}}}}, \quad (9)$$

where the unimproved error e scales as $\propto 1/\sqrt{N_{\text{HP}}}$ and $n_{\text{LP}} = N_{\text{LP}}/N_{\text{HP}}$. r_c is the correlation between the N_{HP} quark propagators in low and high precision, which is expected to be close to unity (with the optimal being one) and depends on the criterion for the LP inversions and on how well-conditioned the Dirac fermion matrix is. In this work, we use the twisted mass formulation for the fermion action, hence the smallest eigenvalues depend on the value of the twisted mass parameter μ , and our matrix is protected from near-zero eigenvalues.

In the TSM one needs to tune the precision of the LP inversions as well as the n_{LP} ratio, with the goal of choosing as large a ratio as possible while still ensuring that the final result is unbiased and that $r_c \simeq 1$. In the next subsection we give details on how we optimized the TSM parameters with this criterion in mind.

1. Tuning the TSM parameters

In order to achieve good performance for the TSM there are two parameters to be tuned, namely the number of noise vectors N_{LP} computed with low precision and the number of noise vectors N_{HP} computed at high precision. The criterion for the low precision inversions can be selected by specifying a relaxed stopping condition in the conjugate gradient, e.g. by allowing a relatively large value of the residual, which will in turn determine the number of iterations required to invert a LP source. Following Ref. [8], we choose a stopping condition at fixed value of the residual $|\hat{r}|_{\text{LP}} \sim 10^{-2}$. N_{HP} is selected by requiring that the bias introduced when using N_{LP} low precision vectors is corrected. Our goal is to develop methods for computing fermion loops with the complete set of Γ -matrices up to one-derivative operators. The tuning is, thus, performed using an operator that requires a large number of stochastic noise vectors, such as g_A or equivalently the nucleon momentum fraction $\langle x \rangle$ and we optimized N_{HP} and N_{LP} so as to get the smallest error at the lowest computational cost.

In Fig. 1 we show the error on the nucleon matrix element of the vector one-derivative operator related to the momentum fraction as a function of N_{LP} for different N_{HP} . For $N_{\text{LP}} = 0$, we observe that the error decreases as the number of HP noise vectors increases, as expected, but saturates when $N_{\text{HP}} = 36$. For $N_{\text{LP}} \neq 0$ we see that the error saturates for $N_{\text{LP}} \gtrsim 200$ for this small test ensemble of 50 configurations, and no further improvement is observed as N_{LP} increases. For $N_{\text{LP}} = 200 - 300$ we observe that we need at least $N_{\text{HP}} = 8 - 12$ to correct the bias or $n_{\text{LP}} \sim 20$. The value of the optimal ratio n_{LP} needed for different loops varies depending on the observable. This is demonstrated in Fig. 2 where we show the

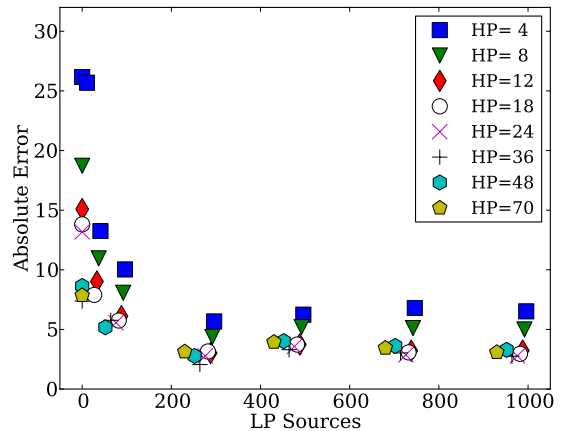


FIG. 1: Tuning of N_{HP} and N_{LP} entering the TSM using the B55.32 ensemble on 50 configurations for the nucleon matrix element of the operator $i\bar{\psi}\gamma_3 D_3\psi$. The insertion time is fixed at $t_{\text{ins}} = 8a$ and sink time at $t_s = 16a$. The error is shown versus N_{LP} for different values of N_{HP} marked by the different plotting symbols as indicated in the legend.

relative error in the case of the isoscalar axial charge g_A and the light quark σ -term, $\sigma_{\pi N} = \frac{m_u + m_d}{2} \langle N | \bar{u}u + \bar{d}d | N \rangle$ for $N_{\text{HP}} = 24$. As can be seen, in the case of g_A one requires at least $N_{\text{LP}} = 500$, while for the $\sigma_{\pi N}$ -term $N_{\text{LP}} = 0$ is sufficient making the TSM unnecessary.

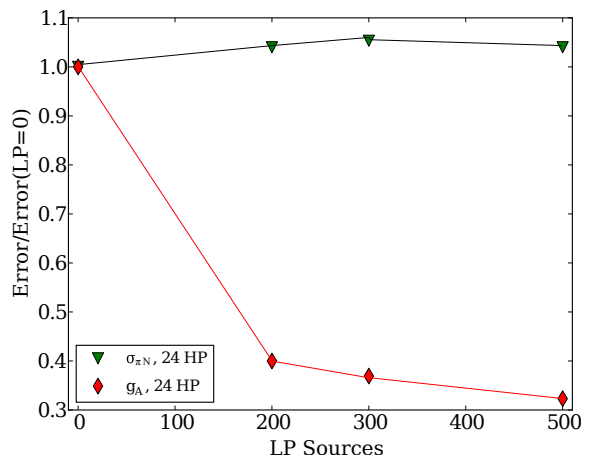


FIG. 2: The error versus N_{LP} fixing $N_{\text{HP}} = 24$ for $\sigma_{\pi N}$ and the isoscalar g_A for 56400 measurements.

In assessing the various methods we will be using $N_{\text{HP}} = 8$ and $N_{\text{LP}} = 200 - 300$. In Fig. 3 we show for $N_{\text{LP}} = 300$ the error on the strange quark loop contribution to the nucleon axial charge g_A^s as a function of N_{HP} . As can be seen, the error remains constant as N_{HP} is increased from 4 to 24. In addition, we show the mean value, which is also consistent for different N_{HP} within the current statistics. Therefore choosing $N_{\text{HP}} = 8$ and $N_{\text{LP}} \leq 300$ does not introduce any bias on the error.

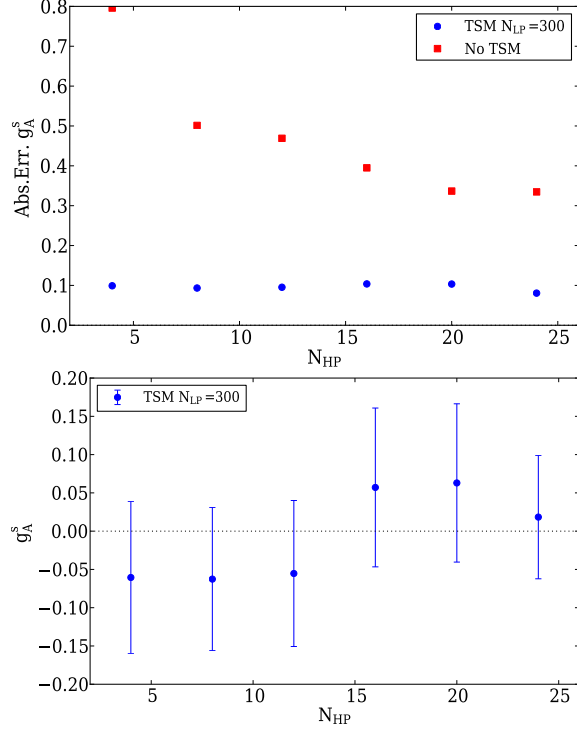


FIG. 3: The error (upper) and the mean value (lower) versus N_{HP} fixing $N_{LP} = 300$ for g_A^s using 448 configurations.

C. The one-end trick

The twisted mass fermion (TMF) formulation allows the use of a very powerful method to reduce the variance of the stochastic estimate of the disconnected diagrams. From the discussion given in section II A, the standard way to proceed with the computation of disconnected diagrams would be to generate N_r stochastic sources η_r , invert them as indicated in Eq. (3), and compute the disconnected diagram corresponding to an operator X as

$$\frac{1}{N_r} \sum_{r=1}^{N_r} \langle \eta_r^\dagger X s_r \rangle = \text{Tr}(M^{-1}X) + O\left(\frac{1}{\sqrt{N_r}}\right), \quad (10)$$

where the operator X is expressed in the twisted basis. However, if the operator X involves a τ_3 acting in flavor space, one can utilize the following identity of the twisted mass Dirac operator with $+\mu$ denoted by M_u and $-\mu$ denoted by M_d :

$$M_u - M_d = 2i\mu a\gamma_5. \quad (11)$$

Inverting this equation we obtain

$$M_u^{-1} - M_d^{-1} = -2i\mu a M_d^{-1} \gamma_5 M_u^{-1}. \quad (12)$$

Therefore, instead of using Eq. (10) for the operator $X\tau_3$, we can alternatively write

$$\begin{aligned} & \frac{2i\mu a}{N_r} \sum_{r=1}^{N_r} \langle s_r^\dagger \gamma_5 X s_r \rangle = \\ & \text{Tr}(M_u^{-1}X) - \text{Tr}(M_d^{-1}X) + O\left(\frac{1}{\sqrt{N_r}}\right) = \\ & -2i\mu a \text{Tr}(M_d^{-1} \gamma_5 M_u^{-1}X) + O\left(\frac{1}{\sqrt{N_r}}\right). \end{aligned} \quad (13)$$

Two main advantages emerge due to this substitution: i) the fluctuations are effectively reduced by the μ factor, which is small in current simulations, and ii) an implicit sum of V terms appears in the right hand side (rhs) of Eq. (12). The trace of the left hand side (lhs) of the same equation develops a signal-to-noise ratio of $1/\sqrt{V}$, but thanks to this implicit sum, the signal-to-noise ratio of the rhs becomes $V/\sqrt{V^2}$. In fact, using the one-end trick yields for the same operator a large reduction in the errors for the same computational cost as compared to not using it [1–3]. The identity given in Eq. 12 can only be applied when a τ_3 flavor matrix appears in the operator expressed in the twisted basis. For other operators one can use the identity

$$M_u + M_d = 2D_W, \quad (14)$$

where D_W is the Dirac-Wilson operator without a twisted mass term. After some algebra, one finds

$$\begin{aligned} \frac{2}{N_r} \sum_{r=1}^{N_r} \langle s_r^\dagger \gamma_5 X \gamma_5 D_W s_r \rangle &= \text{Tr}(M_u^{-1}X) + \text{Tr}(M_d^{-1}X) \\ &+ O\left(\frac{1}{\sqrt{N_r}}\right). \end{aligned} \quad (15)$$

Computing the fermion loops in this way, which we will hereafter refer to as the generalized one-end trick, lacks the μ -suppression factor, which, as we will see, introduces a considerable penalty in the signal-to-noise ratio.

Because of the volume sum that appears in Eq. (12) and Eq. (15), the sources must have entries on all sites, which in turn means that we can compute the fermion loop at all insertions in a single inversion. This allows us to evaluate the three-point function for all combinations of source-sink separation and insertion time-slices, which will prove essential in identifying the contribution of excited state effects for the different operators.

D. Time-dilution

For isovector operators in the twisted mass basis the best approach, as we will discuss in the next section, is

to use the identity given in Eq. (12) that takes advantage of the μ -suppression factor. For other operators the method of choice is not clear and different variance reduction techniques may be more efficient than the generalized one-end trick and need to be considered. One approach that is used to reduce stochastic noise is dilution, i.e. instead of filling up all the entries of the source vector, we populate only parts by decomposing the space $\mathcal{R} = V \oplus \text{color} \oplus \text{spin}$ in m smaller subspaces given by the direct sum $\mathcal{R} = \sum_{i=1}^m \mathcal{R}_i$, and defining our noise sources in those subspaces. This way, Eq. (4) still holds, but a reduction in the variance of the disconnected diagrams may result. This expectation can be seen by examining Eq. (5) where the contributions to the noise come from the off-diagonal terms of M^{-1} , since the matrix $\mathbb{I} - \frac{1}{N_r} \sum_{r=1}^{N_r} |\eta_r\rangle \langle \eta_r|$ features only off-diagonal entries. The off-diagonal terms decrease exponentially with the source-sink separation, so the neighboring terms to the sink have the strongest influence on the errors, hence a dilution in space-time could prove useful in reducing the noise. Noise can also come from strongly coupled spin components, and dilution in color has also been shown to be successful in some systems. In the end, for a given number of subspaces m , whenever the reduction of errors surpasses the factor $1/\sqrt{m}$, dilution becomes advantageous. This cost of inversions can be reduced by using deflated solvers [16, 17], which become more efficient as the number of rhs increases, thereby improving the performance of this approach.

In this work, we examine whether time-dilution can bring an improvement for the operators where Eq. (12) can not be applied. One can apply the coherent method [18, 19] using noise vectors with entries in several time slices, as long as these time slices are far enough from each other, so that only a single loop contributes, thus increasing the statistics at almost no cost. For operators involving a time derivative, one would need additional inversions at time slices $t-1$ and $t+1$ effectively tripling the required computational time. Therefore, for the current work where we focus on comparisons of the different methods, we restrict ourselves to examining ultra-local current insertions, i.e. loops having an insertion of the form $\bar{\psi}(x)\Gamma\psi(x)$.

E. Hopping Parameter Expansion

Another technique that can be used to reduce the variance of our estimate of the propagators is the *Hopping Parameter Expansion* (HPE). The idea is to expand the inverse of the fermionic matrix in terms of the hopping parameter [20],

$$M_u^{-1} = B - BHB + (BH)^2 B - (BH)^3 B + (BH)^4 M_u^{-1}, \quad (16)$$

where $B = (1 + i2\kappa\mu a\gamma_5)^{-1}$ and $H = 2\kappa\mathcal{D}$, with \mathcal{D} the hopping term. The first four terms in this expansion can

be computed exactly, while the fifth term is calculated stochastically as

$$\frac{1}{N_r} \sum_{r=1}^{N_r} [X (BH)^4 s_r \eta_r^\dagger] = \text{Tr} [X (BH)^4 M_u^{-1}] + O\left(\frac{1}{\sqrt{N_r}}\right). \quad (17)$$

The first term in Eq. (16) is the only one that does not involve the gauge links, and is non-zero for ultra-local operators whose γ -structure is proportional to I or γ_5 . The rest of the terms include the hopping matrix, which is traceless, so only the even powers (third term) will survive for ultra-local operators. Moreover, if X is not proportional to I or γ_5 , the third term is zero as well, since the resulting matrix is traceless. For one-derivative operators, only the second and fourth terms survive, provided that X is proportional to either I or γ_5 (or a linear combination of the two). In any case, since these terms are computed in advance and do not depend on the gauge configuration for local operators, they do not incur a serious computational overhead.

III. SIMULATION DETAILS

As already mentioned, we examine the performance of the various methods by analyzing an ensemble of $N_f = 2+1+1$ twisted mass configurations simulated with pion mass of $am_\pi = 0.15518(21)(33)$ and strange and charm quark masses fixed to approximately their physical values (B55.32 ensemble) [21]. The lattice size is $32^3 \times 64$ giving $m_\pi L \sim 5$.

For the disconnected diagrams we make use of a modified version of the QUDA library [22, 23], in which we implement new host code and CUDA kernels to enable the required inversions and contractions on NVIDIA GPUs. In particular, we developed a CUDA version for the twisted-mass fermion operator with even-odd preconditioning to allow QUDA inverters to work with this regularization. We also developed new kernels that carry out efficiently the contractions of the quark propagator and the current insertion, as well as all the interfaces required to make use of these new additions to QUDA. Whereas the new twisted-mass operator is available in the official QUDA release, the contraction kernels are currently available in the local branch of the QUDA git repository, [38]. Details on the implementation of the twisted-mass dslash operator and the new contraction kernels can be found in Appendix A.

For the Fourier transform we use the CUFFT library. The QUDA library allows for inter- and intra-node multi-GPU calculations through MPI; since in our setup there are two GPUs per node, and the GPU-memory requirements for the contractions are high, we use 2 GPUs working in parallel by splitting the lattice between them. In

Figs. 4 and 5 we show strong and weak scaling as a function of the number of GPUs. Strong scaling is good for a few GPUs, with a $\sim 90\%$ increase in performance when adding the second GPU. This result holds for up to 8 GPUs in the strong scaling case, after which we observe a drop in performance. For the architecture on which we carried out these calculations, namely dual M2070 NVIDIA GPU equipped nodes over a QDR infiniband, the only advantage in going beyond 8 GPUs seems to be in the case where GPU memory is insufficient. As can be seen, we can reach TFlop sustained performance with just a few GPUs. Weak scaling on the other hand is almost perfect, which can be understood if one considers that GPUs perform optimally the larger the local lattice size.

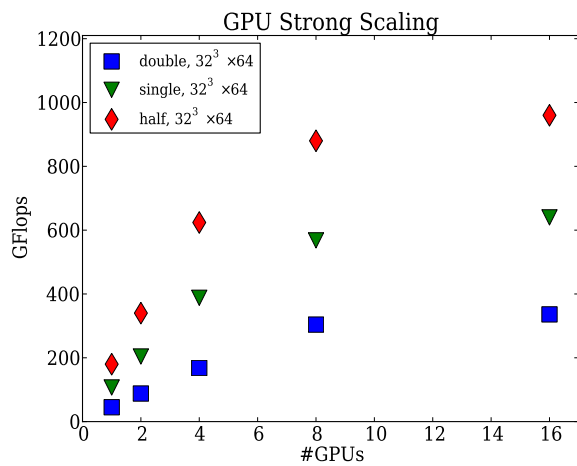


FIG. 4: Strong scaling of the multi-GPU conjugate-gradient solver using the B55.32 ensemble and either 64-bit (double), 32-bit (single) or 16-bit (half) floating point precision.

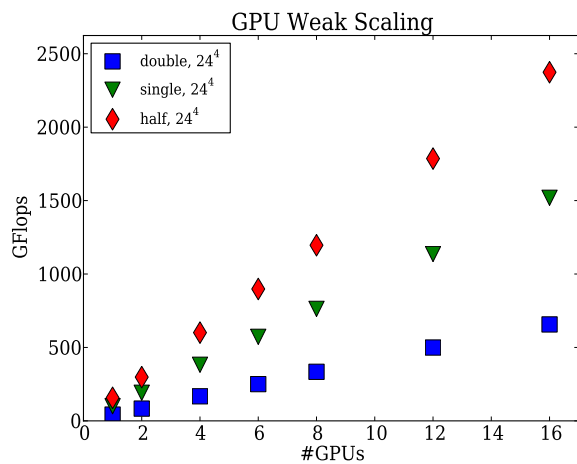


FIG. 5: Weak scaling of the multi-GPU conjugate-gradient solver for a local volume $V = 24^4$, using the same notation as in Fig. 4

The noise sources are generated on-the-fly, and the propagators are not stored, in order to save storage and

I/O time.

IV. ANALYSIS WITH THE PLATEAU AND SUMMATION METHODS

One of the advantages of the one-end trick for twisted mass fermions is the fact that, since the noise sources are defined on all sites, we obtain the fermion loops at all insertion time-slices. We can thus compute all possible combinations of source-sink separations and insertion times in the three-point function. This feature enables us to use the summation method, in addition to the plateau method, with no extra computational effort.

The summation method has been known since a long time [24, 25] and has been revisited in the study of g_A [26]. In both the plateau and summation approaches, one constructs ratios of three- to two-point functions in order to cancel unknown overlaps and exponentials in the leading contribution such that the matrix element of the ground state is isolated. For zero-momentum transfer we consider the ratio

$$R(t_{ins}, t_s) = \frac{G^{3pt}(t_{ins}, t_s)}{G^{2pt}(t_s)}, \quad (18)$$

where $G^{3pt}(t_{ins}, t_s)$ and $G^{2pt}(t_s)$ are the three- and two-point functions at zero momentum, respectively. The leading time dependence of this ratio is given by

$$R(t_{ins}, t_s) = R_{GS} + O(e^{-\Delta E_K t_{ins}}) + O(e^{-\Delta E_K (t_s - t_{ins})}), \quad (19)$$

where R_{GS} is the matrix element of interest, and the other contributions come from the undesired excited states of energy difference ΔE_K . In the plateau method, one plots $R(t_{ins}, t_s)$ as a function of t_{ins} , which should be a constant (plateau region) when excited state effects are negligible. A fit to a constant in the plateau region thus yields R_{GS} . In the alternative summation method, one performs a sum over t_{ins} to obtain:

$$R_{sum}(t_s) = \sum_{t_{ins}=0}^{t_{ins}=t_s} R(t_{ins}, t_s) = t_s R_{GS} + a + O(e^{-\Delta E_K t_s}) \quad (20)$$

and now the exponential contributions coming from the excited states decay as $e^{-\Delta E_K t_s}$ as opposed to the plateau method where excited states are suppressed like $e^{-\Delta E_K (t_s - t_{ins})}$, with $0 \leq t_{ins} \leq t_s$, the insertion time. Therefore, we expect a better suppression of the excited states for the same t_s . Note that one can exclude from the summation $t_{ins} = t_s$ and $t_{ins} = 0$ without affecting the dependence on t_s in Eq. (20). The results given in this work are obtained excluding these contact terms from the summation. The drawback of the summation method is that one requires knowledge of the three-point function for all insertion times and that we need to fit to a straight line with two fitting parameters instead of one.

V. COMPARISON OF RESULTS OF DIFFERENT METHODS

In order to compare the various methods, we focus on two quantities with very different behaviors: the σ -term, for which the stochastic noise is small and thus a relatively small number of noise sources are required, and g_A that belongs to a class of observables which require a large number of noise vectors and statistics to be computed in a reliable way. These two quantities are also different with respect to excited states contamination, with the σ -terms having large excited state contributions [27, 28] while g_A was shown to be less affected [29, 30], although the degree of contamination may depend on the value of the pion mass [31–33]. We note in particular that the summation method as applied in the extraction of g_A in Ref. [33] led to agreement with the physical value after performing a chiral extrapolation, while in Ref. [31] it was shown that the value extracted using the summation method at near physical pion mass is reduced further away from the physical value, possibly due to thermal effects [32]. On the other hand, a high statistics analysis for the ensemble used in this work showed no excited states contamination for g_A [29], while for the σ -term for the same ensemble we find large contributions from excited states. We expect the excited states contribution to behave similarly for the connected and disconnected three-point functions. This has been verified in the case of the nucleon $\sigma_{\pi N}$ as shown in Fig. 6 where we show both the connected and disconnected contributions.

In this work we evaluate the light disconnected contributions, the strange and charm quark contributions to both of these observables with the one-end trick. In addition, we calculate the strange quark contribution when using time-dilution, both with and without the HPE and compare the results. Regarding the renormalization of the σ -terms, the twisted mass formulation has the additional advantage of avoiding any mixing, even though we are using Wilson-type fermions [3]. For the case of the axial charge, renormalization involves mixing from the three quark sectors. For the tree-level Symanzik improved gauge action this mixing was shown to be a small effect of a few percent [34]. We expect this to hold also for the Iwasaki action used in this work. Since the main goal of this paper is the comparison of methods, we renormalize the axial charge neglecting any mixing using the same renormalization constant as the purely connected part, that is, by multiplying by Z_A .

A. Efficiency of TSM

We first examine the performance of TSM for the σ -term. In Fig. 7 we show the disconnected contributions for $\sigma_{\pi N}$, the strange $\sigma_s = \mu_s \langle N | \bar{s}s | N \rangle$ and charm $\sigma_c = \mu_c \langle N | \bar{c}c | N \rangle$ nucleon σ -terms. The strange and charm σ -terms are computed using Osterwalder-Seiler

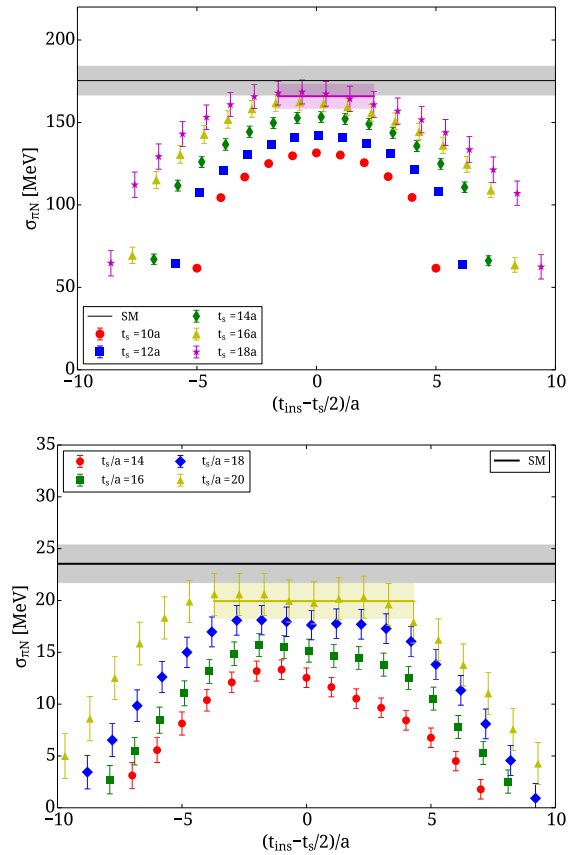


FIG. 6: Excited states contribution to the connected (upper) and disconnected (lower) ratios for $\sigma_{\pi N}$. The ratio is shown as a function of the insertion time-slice with respect to mid-time separation $(t_{\text{ins}} - t_s/2)$ for various source-sink separations, t_s . The gray band is the result obtained from the summation method while the colored band is the result of the constant fit in the plateau region.

fermions with μ_s and μ_c tuned to reproduce the kaon and D-meson masses of the unitary theory. Results are obtained using the one-end-trick with and without applying the TSM. For the case where we employ TSM, we use $N_{\text{LP}} = 200$ for loops containing light quarks and $N_{\text{LP}} = 300$ for strange and charm quark loops. These choices for N_{LP} yield approximately the same statistical errors allowing a more direct comparison of computer time. Namely, for the case of $\sigma_{\pi N}$, we obtain results with similar errors but with reduced computational cost for the TSM by $\sim 34\%$ showing that the TSM is preferable. As the quark mass increases, the computational cost for the TSM for similar errors becomes comparable to that of using only HP inversions. Thus for σ_s the TSM is comparable to only using $N_{\text{HP}} = 24$. For even heavier masses such as in the case of the charm quark the use of the TSM is not justified since the computer time increases by a factor of 5, while the errors are reduced by a mere $\sim 33\%$. Thus, when the inversion of the Dirac matrix is fast as in the case of the charm quarks there is not much benefit from using lower precision. Rather the in-

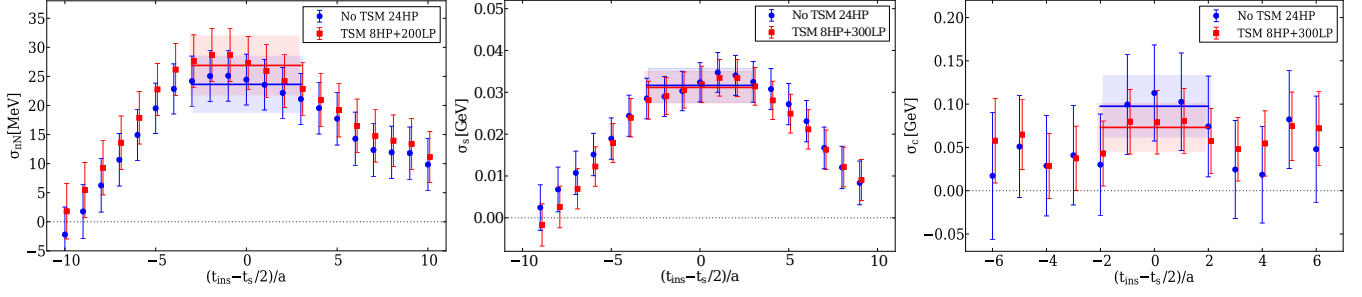


FIG. 7: Comparison of results obtained using $N_{\text{HP}} = 24$ with $N_{\text{LP}} = 0$ (no TSM) with those obtained using the TSM for $N_{\text{HP}} = 8$ and $N_{\text{LP}} = 300$, except for the light sector, which uses $N_{\text{LP}} = 200$. Left panel: the disconnected contribution to $\sigma_{\pi N}$ with a total of 56400 measurements; central panel: σ_s with a total of 58560 measurements; and right panel: σ_c with a total of 58560 measurements. All results are obtained using the one-end trick.

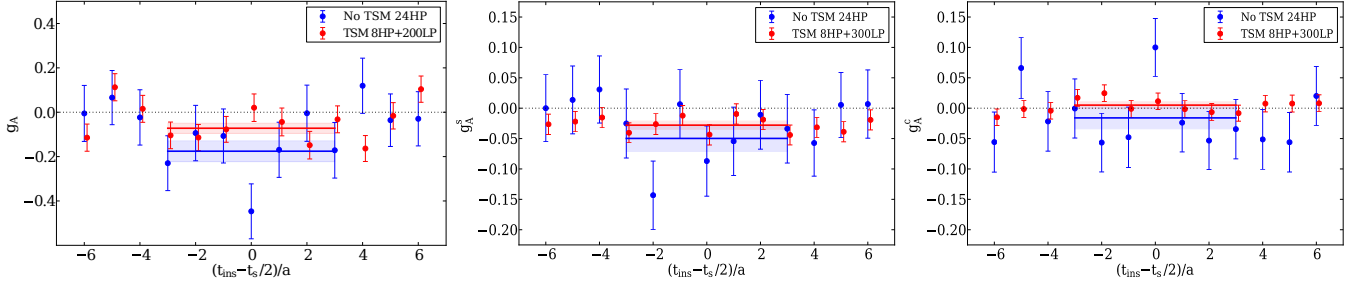


FIG. 8: The same as in Fig. 7 but for the disconnected contributions to the nucleon axial charge.

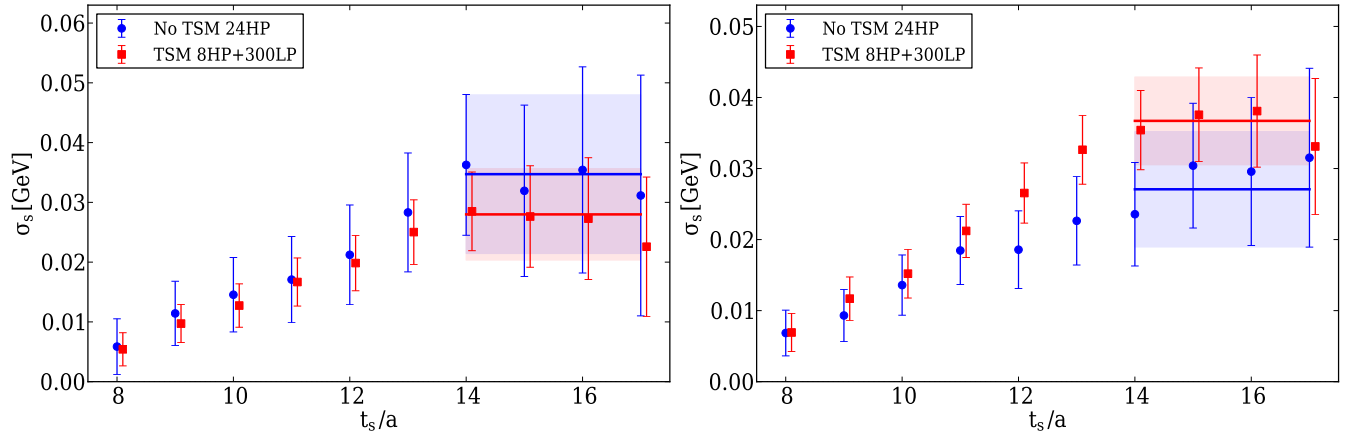


FIG. 9: Results for the ratio from which σ_s is extracted versus the sink time separation t_s when using only $N_{\text{HP}} = 24$ (no TSM) to those obtained when using $N_{\text{HP}} = 8$ and $N_{\text{LP}} = 300$. Results are obtained using time-dilution (left panel) and time-dilution plus HPE (right panel). In all cases the insertion-source separation $t_{\text{ins}} = 8a$ and a total of 18628 measurements are performed.

creased number of contractions required when using the TSM, which is a constant overhead independent of the quark mass, becomes more significant than any speed-up obtained by using lower-precision inversions.

We perform the same analysis for g_A , which has a different convergence pattern as compared to the σ -terms. Contrary to the case of the σ -terms, for g_A one must use the generalized version of the one-end trick since computing the isoscalar axial charge in the twisted basis requires summing the quark-flavor contributions. In Fig. 8 we show results for the disconnected light quark contributions to g_A , the strange and charm contributions to the nucleon axial charge denoted by g_A^s and g_A^c respectively. As can be seen, there is an improvement when using the TSM for all quark masses, though the improvement is more significant the lighter the quark mass is. In the most favorable case, i.e. that of the light quark sector, we see more than a two-fold reduction in the error when using the TSM for about 66% of the computational cost. In the case of g_A^c , although the TSM is computationally more demanding by a factor of 5 for the chosen parameters of the plot, the four-fold reduction in the error overcompensates for this cost.

We next assess the performance of the TSM in combination with time-dilution instead of with the one-end trick as done above for the same two observables considered. The comparison is performed for the strange quark fermion loops in order to speed-up the computations. Time-dilution also allows straightforward application of the HPE method, which potentially can lead to improvement in particular for heavier quark masses. As already explained, the overhead in computer time when applying the HPE is insignificant, since it essentially requires a few applications of the Wilson-Dirac operator. In Fig. 9 we show the results for the ratio from which σ_s is extracted using $N_{\text{HP}} = 24$ high precision inversions and $N_{\text{LP}} = 0$ compared to those obtained when using the TSM with $N_{\text{HP}} = 8$ and $N_{\text{LP}} = 300$. The computational cost in the two cases is roughly the same. As can be seen, the TSM yields smaller errors by about a factor of two both with and without the HPE. For the case of g_A^s shown in Fig. 10 the results are even more favorable for the TSM, where one obtains the right long time behavior even when the HPE is not applied. Using time dilution with $N_{\text{HP}} = 24$ only we obtain the wrong results indicating that no convergence has been reached. The TSM yields better than a two-fold reduction in errors for the same computer time yielding results consistent with those obtained using the one-end trick. Thus, applying the HPE leads to improvement and it should be employed when using time-dilution.

It is helpful to directly compare the results obtained with time-dilution and the TSM with and without the HPE. As explained, applying the HPE comes with almost no computational cost. A direct comparison is shown in Fig. 11. As can be seen, errors are reduced by about a factor of two in the case of g_A^s when using the HPE. Moreover, we expect a greater improvement as the quark

mass becomes heavier. Since the addition of HPE improves results without increasing the computer time in a noticeable way, it is always advantageous to use it for quark masses in the range of the strange quark or heavier.

It is important to stress that the creation of stochastic sources, the inversions and all contractions are carried out on GPUs such that the communication between CPU and GPU is reduced. In order to do that, the sources are directly contracted on the GPUs right after the inversion, the calculated propagators are discarded, and only the contractions are transferred to the CPUs to be stored on disk [35].

Even with such a setup, for quark masses larger than the strange quark mass the differences in computer time between high and low precision inversions become small as compared to the time spent for contractions to calculate the loop. This is due to the fact that the pre- and post-processing computational costs are independent of the quark mass and therefore more time consuming for the TSM where an order of magnitude more noise vectors are used, thus reducing the improvements observed by the TSM for the case of heavy quarks. In Table I we give a summary of the computer time required for the computation of fermion loops within the various methods. We give the ratio $R_{\text{HP/LP}}$ of the computer time required to compute a fermion loop for one noise vector using HP to the time needed to compute the loop using LP, taking into account the time for the inversion as well as the pre- and post-processing time (creation of sources, performing the contractions and taking the traces). A large value for this ratio indicates that the TSM is more efficient, since more LP vectors can be used for the computation of the loops as compared to the cost of a loop using one HP inversion. A value close to unity indicates that the TSM is no longer advantageous, since in such a case one can exchange LP inversions for HP with the same cost. For the case of the strange quark loops with local operator insertion $R_{\text{HP/LP}} \gg 1$ when time-dilution is applied either with or without HPE. In the case of using the one-end trick to compute the fermion loops the TSM has a better performance for both ultra-local and one-derivative operator insertions for light and strange quarks. As the quark mass increases, $R_{\text{HP/LP}}$ decreases making the TSM less advantageous for charm quarks.

We note here that we have not carried out an analysis of time-dilution for the case of derivative insertion operators, since one would require to include fermion loops computed at three time-slices to take the time derivatives, which would effectively triple the cost of time-dilution.

Our main conclusion from the comparison carried out in this section is that the TSM is the method of choice for light quarks and for the case of operators where the generalized one-end trick is used. In the charm quark mass range with our current implementation on GPUs the TSM becomes less efficient since the pre- and post-processing overheads become large as compared to the inversion time. For observables like g_A the TSM is still

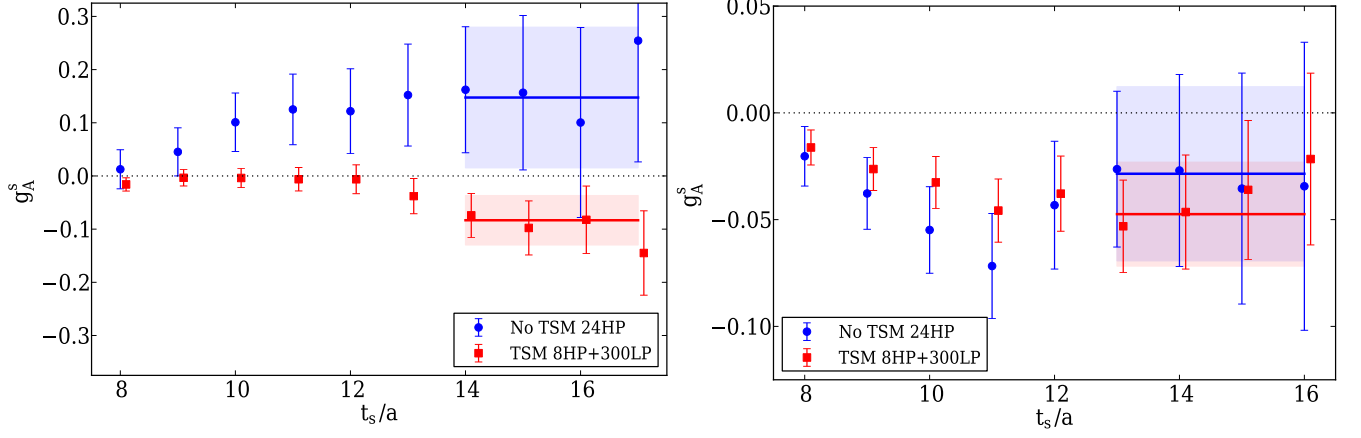


FIG. 10: The same as in Fig. 9 but for the case of g_A^s .

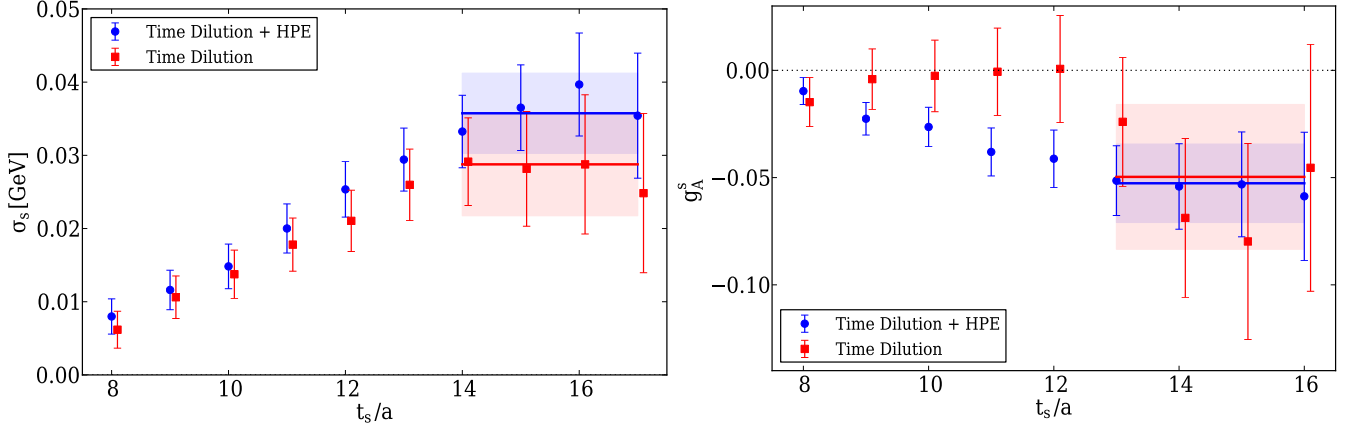


FIG. 11: Comparison of results for the ratio from which σ_s (left panel) and g_A^s (right panel) are extracted using time-dilution in combination with the TSM with and without application of the HPE. A total of 18628 measurements are used.

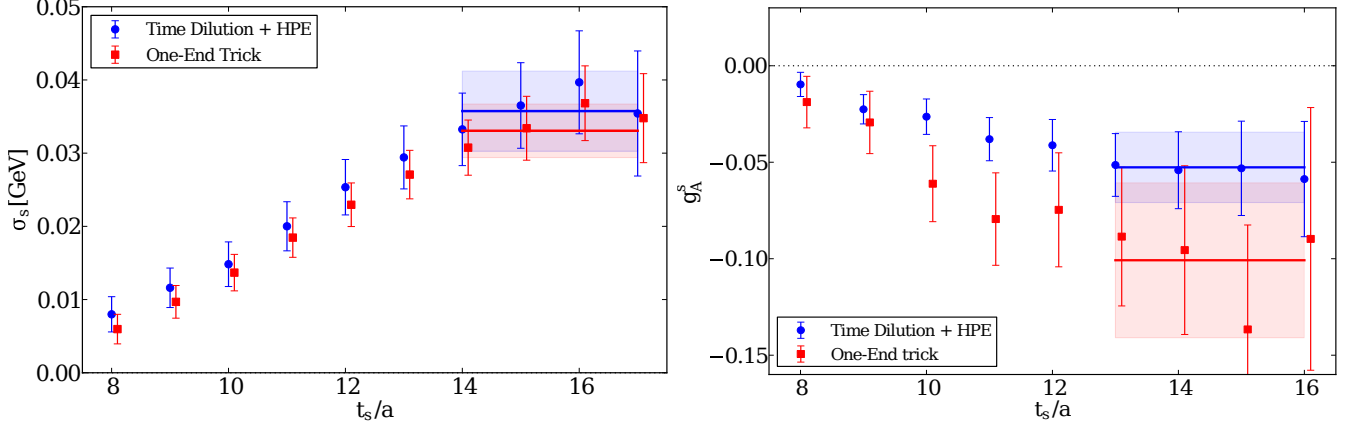


FIG. 12: Results for the ratio from which σ_s (left) and g_A^s (right) are extracted. With filled (blue) circles are results obtained using the one-end trick and with filled (red) squares when using time-dilution. In both cases we use the TSM with $N_{\text{HP}} = 24$ and $N_{\text{LP}} = 300$ and 18628 measurements. The current insertion is fixed at $t_{\text{ins}} = 8a$.

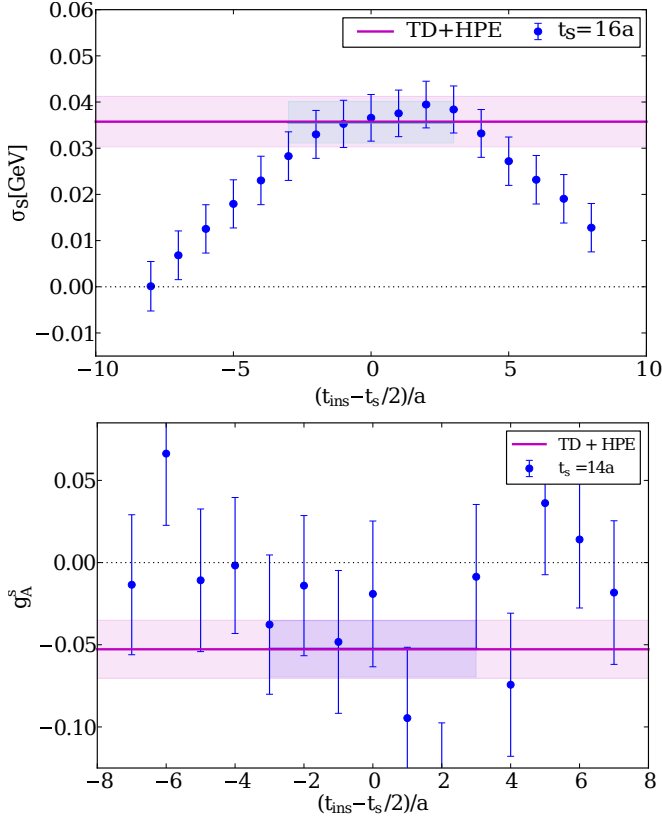


FIG. 13: Ratios for σ_s at $t_s = 16a$ (top) and g_A^s at $t_s = 14a$ (bottom) obtained using the one-end trick. The purple band shows the result of fitting the asymptotic behavior of the ratio obtained with time-dilution. The TSM with $N_{\text{HP}} = 24$ and $N_{\text{LP}} = 300$ is used in both methods with 18628 statistics.

Method	Quark sector	$R_{\text{HP/LP}}^{\text{Local}}$	$R_{\text{HP/LP}}^{\text{One-Deriv.}}$
One-end trick	Light	~ 26.7	~ 10
One-end trick	Strange	~ 16.9	~ 5.8
One-end trick	Charm	~ 2.9	~ 1.4
Time-dil.	Strange	~ 20.7	—
Time-dil. + HPE	Strange	~ 19.1	—

TABLE I: Computational cost when using TSM with the one-end trick or with time-dilution for different quark masses. The third column is the ratio of the cost for computing a fermion loop using a HP inversion to a low precision one, including inversion time and time for pre- and post-processing for ultra-local operator insertions. The fourth column gives the corresponding ratio when including one-derivative operators to the ultra-local ones.

superior for computing strange quark loops and remains an equally good option for charm quark loops. For the σ -terms the one-end trick works very well and the TSM is not necessary. However, since our goal is to compute all loops at once the TSM is the method of choice for obtaining high statistics results if one wants to compute all the disconnected contributions to observables probing nucleon structure.

B. Time-dilution plus HPE vs the one-end trick

In the previous section we compared results obtained using the one-end trick as well as time-dilution with and without the TSM and the HPE. Here we employ the TSM with $N_{\text{HP}} = 24$ and $N_{\text{LP}} = 300$ and compare results obtained with the one-end trick to those obtained using time-dilution with HPE. In Fig. 12 we show results for the ratio from which σ_s and g_A^s are extracted. The ratio is plotted as a function of the sink-source separation t_s for fixed current insertion time $t_{\text{ins}} = 8a$. In the case of σ_s results obtained using the one-end trick of Eq. (13) are compared to those obtained using time-dilution and HPE, whereas for g_A^s the generalized one-end trick of Eq. (15) is compared to time-dilution and HPE. As can be seen, for σ_s the one-end trick yields smaller errors than time-dilution for the same statistics. On the other hand, for g_A^s time-dilution yields smaller errors. However, in the case of the one-end trick one obtains the fermion loops at all time-slices without any further inversions, while when using time-dilution the fermion loop is calculated at a single time-slice or at up to four in our setup when using the coherent source method. As a consequence, with the one-end trick we can obtain results for all current insertions *and* for multiple sink-source time separations. Thus one can fit the plateau as shown in Fig. 13 and compare with the result extracted when using time-dilution at fixed t_{ins} . Fitting the plateau for g_A^s yields a result with the same error as that obtained using time-dilution. Thus, this comparison shows that the one-end trick is preferable for the calculation of fermion loops even when the generalized form of Eq. (15) is used.

An additional advantage of the one-end trick is that having results for multiple sink-source time separations allows for the assessment of excited state contributions as well as for applying the summation method with no extra inversions. In contrast, time-dilution requires an inversion for every new insertion time, which would effectively multiply the computational cost by the number of time-slices between source and sink of the largest separation considered. Furthermore, with the one-end trick one has the loop at all time-slices which allows coupling the loop to multiple two-point functions computed with different source positions. The two-point functions at each new source position require new inversions, however the loops are computed once with the one-end trick at all time-slices, thus multiplying the number of statistics at the cost of regular point-to-all inversions. The advantage of having multiple sink-sources separations is demonstrated for the strange σ -term (σ_s) and strange-quark contribution to the axial charge (g_A^s) shown in Figs. 14 and 15 respectively. In both cases we computed 16 two-point functions per configuration on 2,300 gauge-field configurations resulting in 147,200 statistics since we average forwards and backwards propagating nucleons and proton and neutron channels. For this high statistics analysis we take $N_{\text{HP}} = 24$ and $N_{\text{LP}} = 300$. As can be seen in Figs. 14 and 15, the multiple sink-source time sepa-

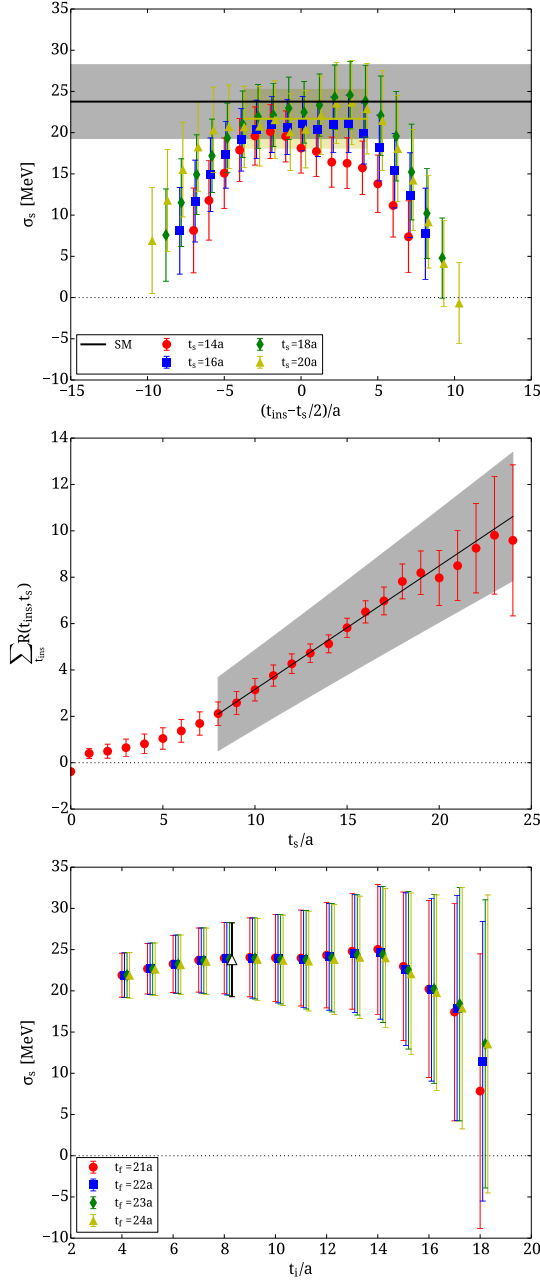


FIG. 14: Comparison of the summation and the plateau methods for σ_s . In the upper panel we show the ratio as a function of the insertion time-slice with respect to mid-time separation $(t_{\text{ins}} - t_s)/2$ for source-sink separations, $t_s = 14a$ (red circles), $t_s = 16a$ (blue squares), $t_s = 18a$ (green rhombuses) and $t_s = 20a$ (yellow triangles). In the middle panel we show the summed ratio, for which the fitted slope yields the desired matrix element. In the bottom panel we show the results obtained for the fitted slope of the summation method for various choices of the initial and final fit time-slices. The open triangle shows the choice for which the gray bands are plotted in the upper and middle panels.

rations are crucial in probing excited states contamination. The summation method, which serves as a different

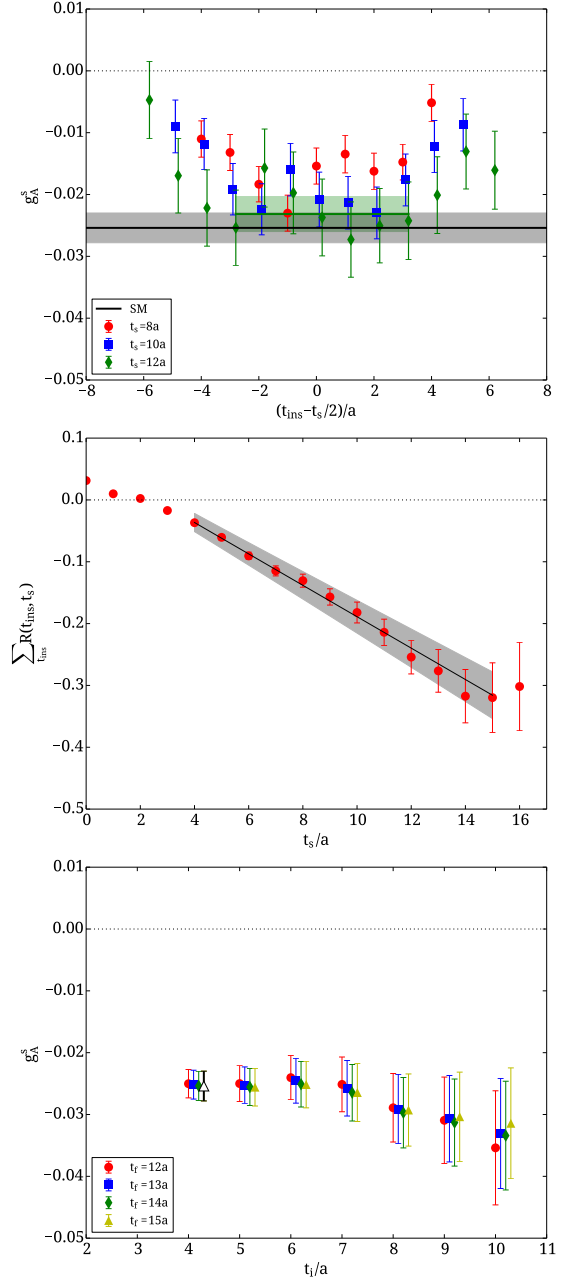


FIG. 15: Comparison of the summation and the plateau methods for the strange contribution to the axial charge: g_A^s . In the upper panel we show the ratio as a function of the insertion time-slice with respect to mid-time separation $(t_{\text{ins}} - t_s)/2$ for source-sink separations, $t_s = 8a$ (red circles), $t_s = 10a$ (blue squares) and $t_s = 12a$ (green rhombuses). The rest of the notation is the same as that of Fig. 14.

way of extracting the observable, can only be applied if we have these multiple sink-source time separations. Although a noticeable improvement in statistical accuracy is not obtained when using the summation method, it is very useful as an additional check of convergence to the ground state, especially for the case of the σ -term where excited state effects appear to be larger.

We have carried out a comparison between time-dilution with HPE and the one-end trick only for strange quark loops. We expect the one-end trick to perform better for light quarks since HPE is less suited, while for heavier masses time-dilution combined with HPE may become advantageous due to the HPE. Another reason to favor the one-end trick method is for the case of one-derivative operators. To compute such derivative operators in time one requires the fermion loops at at least three neighboring time-slices. For the one-end trick this requires no further inversions since one obtains the loops at all time-slices, however for time-dilution, where an inversion is required at every time-slice, this triples the computational cost.

C. Summary on the performance of the various methods

We summarize the outcome of the comparisons in Table II where we give the computational cost and relative error for the disconnected diagrams contributing to the σ -terms and the axial charges for the light, strange and charm quarks. A measure of the comparative cost is given in seconds of computer time per configuration on two Tesla M2070 GPUs. Since all operator insertions in the loop of a given quark flavor are computed simultaneously, the cost for different observables is the same when using the same method. To make the comparison meaningful, we restricted the number of two-point functions used, so the statistics in all cases are 18628 measurements. The entry in the last column gives the comparative advantage of each method [36].

From Table II it is clear that the one-end trick plus TSM is the most suitable method for computing the disconnected contributions to $\sigma_{\pi N}$ and g_A . Since these observables have very different convergence properties, we conclude that this method will be preferable for the disconnected contributions due to the light quark loops for other observables. For the strange quark loops we have performed also a comparison with time-dilution. As can be seen from the $\text{error}^2 \times \text{cost}$, the one-end trick plus TSM is also the preferred method over time-dilution plus any combination of TSM and/or HPE. For the charm quark loops the one-end trick performs better as compared to including the TSM for σ_c . However, including the TSM clearly reduces the cost for a fixed error in the case of g_A^c . Thus, since for a class of observables one needs to use the TSM, using it also for the computation of σ_c comes with no cost.

VI. CONCLUSIONS AND OUTLOOK

The computation of disconnected contributions for flavor singlet quantities has become feasible, due to the development of new techniques to reduce the gauge and stochastic noise, and due to the increase in computa-

Method	Abs. Error	OH	Cost	Cost \times Error ²
$\sigma_{\pi N}$				
One-end trick	4.3 MeV	65	2234	0.032
One-end trick + TSM	3.8 MeV	290	1471	0.027
σ_s				
One-end trick	5.1 MeV	65	754	0.019
One-end trick + TSM	4.9 MeV	409	809	0.019
Time-dil.	13 MeV	31	745	0.126
Time-dil. + TSM	7.5 MeV	281	710	0.040
Time-dil. + HPE	8.0 MeV	34	750	0.048
Time-dil. + HPE + TSM	6.2 MeV	322	750	0.029
σ_c				
One-end trick	95 MeV	65	144	1.30
One-end trick + TSM	61 MeV	409	692	2.57
g_A				
One-end trick	0.19	65	2234	80.6
One-end trick + TSM	0.081	409	1471	9.65
g_A^s				
One-end trick	0.076	65	754	4.36
One-end trick + TSM	0.023	409	809	0.43
Time-dil.	0.132	31	721	5.08
Time-dil. + TSM	0.049	281	676	1.62
Time-dil. + HPE	0.040	34	725	1.16
Time-dil. + HPE + TSM	0.024	322	692	0.40
g_A^c				
One-end trick	0.076	65	144	0.83
One-end trick + TSM	0.0215	409	692	0.32

TABLE II: Comparative computational cost for the σ -terms and axial charges using the different methods. The cost, in units of GPU-node seconds (2 GPUs per node), is given for the computation of the quark loop for one configuration, using $N_{\text{HP}} = 24$, $N_{\text{LP}} = 0$ and $N_{\text{HP}} = 8$ and $N_{\text{LP}} = 200$ or $N_{\text{LP}} = 300$ depending on the quark mass, as discussed above. For a fair comparison we used the same statistics, namely 18628 measurements, for time-dilution and the one-end trick. The sink was set at $t_s = 16a$ for the one-end trick data, and the insertion to $t_{\text{ins}} = 8a$ for time-dilution. The column labeled as OH represents what we call the *overhead*, in other words, the time of pre- and post-processing employed in generating the disconnected quark loops, whereas the cost includes the inversion time as well. It can be seen how the overhead time depends only on the number of sources calculated (not on the mass), and it becomes more and more important, as the matrix inversions become faster, that is, for larger quark masses. The last column defines a quantity that is independent of statistics, which gives the comparative cost for a fixed error of a given observable [36].

tional resources. In this work, we explore a number of recent developments for the determination of disconnected contributions to hadron matrix elements. The usage of GPUs is particularly important, due to its efficiency in the evaluation of disconnected diagrams using the TSM, since GPUs can yield a large speedup when employing single- and half-precision for the computation of the LP inversions and associated contractions.

Among all the algorithms analyzed, the one-end trick

seems to perform better in most cases, reducing the variance of the disconnected loops at the same computational cost for many flavor-singlet quantities. It also delivers the fermion loops for all the possible insertion times at no extra cost, so we can use the summation method in the analysis, and the computation of one-derivative insertions is straightforward, whereas for the case of time-dilution, several separated inversions must be performed.

The TSM can improve the efficiency of the one-end trick for quark masses up to the strange quark mass. For heavier masses, the performance of the TSM degrades, and depending on the disconnected quark loop to be computed it is no longer beneficial. In our case, we observe a performance degradation for σ_c but a clear improvement for g_A^c yielding results with smaller errors. Thus for loops where the stochastic noise is expected to be large the TSM still performs better even for heavy quark masses where the CG converges fast.

In a follow-up paper we will apply the TSM to perform a high statistics analysis of the disconnected diagrams involved in observables probing nucleon structure. These will include the isoscalar electromagnetic and axial vector form factors, the sigma-terms, the momentum fraction and helicity.

Acknowledgments

A. V. and M. C. are supported by funding received from the Cyprus Research Promotion Foundation (RPF) under contracts EPYAN/0506/08 and TECHNOLOGY/ΘΕΠΠΣ/0311(BE)/16 respectively. K. J. is partly supported by RPF under contract ΠΡΟΣΕΛΚΥΣΗ/ΕΜΠΕΙΡΟΣ/0311/16. This research was in part supported by the Research Executive Agency of the European Union under Grant Agreement number PITN-GA-2009-238353 (ITN STRONGnet) and the infrastructure project INFRA-2011-1.1.20 number 283286 (HadronPhysics3), and the Cyprus RPF under contracts KY-ΓΑ/0310/02 and NEA ΥΠΟΔΟΜΗ/ΣΤΡΑΤΗΓ/0308/31 (infrastructure project Cy-Tera, co-funded by the European Regional Development Fund and the Republic of Cyprus through RPF). Computational resources were provided by the Cy-Tera machine and Prometheus (partly funded by the EU FP7 project PRACE-2IP under grant agreement number: RI-283493) of CaStoRC, Forge at NCSA Illinois (USA), Minotauro at BSC (Spain), and by the Jugene Blue Gene/P machine of the Jülich Supercomputing Center awarded under PRACE.

Appendix A: Details on the implementation of the GPU code

1. Twisted mass fermion operator

In this section we provide some implementation aspects of the twisted mass code development in QUDA. The Wilson twisted mass fermion operator formulation for the degenerate flavor doublet reads:

$$\mathbb{D}_{TM} = \mathbb{D}_W + i\mu\gamma_5\tau^3, \quad (\text{A1})$$

where \mathbb{D}_W stands for the Wilson term, τ^3 denotes the diagonal $SU(2)$ Pauli matrix and μ is the (bare) twisted mass parameters. For internal computations QUDA adopts a non-relativistic basis for the spinor projections; this allows to reduce memory traffic while computing hopping terms in time direction [22].

For the QUDA twisted mass iterative solvers one can employ two types of (even-odd) preconditioning: symmetric and asymmetric. For instance, one may deal with the following equivalent ('even-even') preconditioned systems:

$$(R_{ee} - \kappa^2 \mathbb{D}_{eo} R_{oo}^{-1} \mathbb{D}_{oe}) \psi_e = b_e - \mathbb{D}_{eo} R_{oo}^{-1} b_o \quad (\text{A2})$$

$$(I_{ee} - \kappa^2 R_{ee}^{-1} \mathbb{D}_{eo} R_{oo}^{-1} \mathbb{D}_{oe}) \psi_e = R_{ee}^{-1} (b_e - \mathbb{D}_{eo} R_{oo}^{-1} b_o) \quad (\text{A3})$$

where R represents a local twisting operator and the odd component of the solution is reconstructed by the expression:

$$\psi_o = R_{oo}^{-1} (b_o - \mathbb{D}_{oe} R_{ee}^{-1} \psi_e). \quad (\text{A4})$$

Accordingly, we implemented a number of 'fused' CUDA kernels, such as $R_{oo}^{-1} \mathbb{D}_{oe}$, $(R_{ee} - \kappa^2 \mathbb{D}_{eo})$ (and their 'daggered' analogues), required for the left-hand-side of Eq. (A.2). As a result, all local operators are merged into dslash kernels and computed on the fly reducing expansive accesses to the GPU global buffer. All these kernels are generated by a python script in the same way as it is done for other fermion operators available in QUDA.

Finally, to include the twisted mass dslash operator in the whole framework, we added two new classes, `DiracTwistedMass` and `DiracTwistedMassPC`, which encapsulate all necessary attributes and methods for launching dslash kernels on the accelerators. The multi-GPU parallelization for the degenerate flavor doublet is almost identical to the corresponding Wilson implementation. The only difference consists in the necessity to apply the local twisting operator R^{-1} (e.g., entering operators in the lhs of Eq. (A3)) while gathering boundary-spinor sites: we provided with an extra packing routine to properly take into account this case. More detailed information about optimization strategies exploited in the QUDA library can be found in Refs. [22, 23, 37].

We adduce single-GPU performance summary for the asymmetrically preconditioned dslash operator on the

TABLE A.1: Single GPU performance in GFlops.

Prec.	Recon.	Wilson	Degenerate TM
double	12	184	190
	8	179	183
single	12	401	415
	8	472	487
half	12	732	759
	8	829	858

NVIDIA GTX Titan card. Here we included the plain Wilson case as a reference point. The lattice size for the single-GPU runs was 32×64 and we examined two types of gauge field reconstructions, namely 8- and 12-parameter reconstructions. QUDA allows for storing the gauge-field links in less than the 9 complex numbers needed to store a full $SU(3)$ matrix. In one case, it allows omitting one row of the three, reducing the storage requirements to 6 complex numbers, so-called 12-parameter reconstruction. With 8-parameter reconstruction, the link is decomposed into a linear combination of the eight $SU(3)$ generators and only the coefficients are stored (8 real numbers). In both cases the full $SU(3)$ is recomputed on the fly during the Dirac operator application. This reduces both the memory requirements but more importantly the bandwidth requirements of applying the Dirac matrix. In addition, to benefit from full-clock speed for the double precision Arithmetic Logic Units on the gaming card we set

`GPUDoublePrecisionBoostImmediate=1.`

We summarize our results in Table A.1.

2. Contraction kernels

A fundamental step in the calculation of quark loops is the contraction of inverted sources. To this end we developed efficient GPU code yielding ~ 300 GFlops in a single Tesla m2070 GPU in double precision, and showing almost perfect scaling with increasing number of GPUs.

Traces were taken in color space, leaving the Dirac and volume indices open. The volume indices are used later for the FFT, so we obtain solutions for different momenta, whereas the open Dirac indices are there in order to deal with the different insertions. We calculated the outer product in Dirac space of both sources to be contracted, and consequently a 4×4 matrix was obtained, with enough information to reconstruct any arbitrary γ insertion just by transposition and multiplication. Therefore, our contraction code automatically outputs all the possible insertions for ultra-local operators. A covariant-derivative kernel was also developed to allow the calculation of one-derivative insertions.

These GPU kernels were developed in two different versions: whole spinor contraction (for the one-end trick) and single time-slice contraction (for time-dilution). The

single time-slice contraction kernel does not support at this moment the inclusion of the covariant-derivative, for this would imply to deal with several time-slices at the same time.

3. Interfaces and workflow

Since QUDA already implements most of the code we need for computing disconnected diagrams, the largest contribution to the library on this package is the writing of interfaces. Those were designed to calculate any ultra-local and one-derivative insertion with several variance reduction methods, namely the TSM, the one-end trick (only for twisted mass fermions), time-dilution and the Hopping Parameter Expansion, and all the possible combinations of these.

The interface generates random stochastic sources using RANLUX from the GSL library on the CPUs; then the source is sent to the GPUs for inversion and contraction, and contractions are stored back in the CPUs. This process is repeated several times for the binary storage system, explained below. After we accumulated enough sources, the data is sent back from CPUs to GPUs for FFT using the NVIDIA library cuFFT; our output from the last section fits exactly in the input required in the functions of the cuFFT library, so no further transformations are required. At this point, all possible momenta are generated, but we usually insert here a cut-off in p^2 to reduce storage. Finally, the results are written to disk in a parallel fashion to reduce I/O time.

4. Binary storage system

When the TSM is introduced, one has to face the problem of storage and take decisions regarding which information can be discarded, due to the large number of stochastic sources generated. In our case it was decided that only contractions would be stored, but even in this case a storage problem might appear.

For instance, if we decide to use volume sources in our calculation (i.e. we are using the one-end trick), our code will compute all ultra-local and one-derivative insertions, with and without a flavor τ_3 matrix, that is, 160 insertions in total. We impose a momentum cut-off that we can set in our example to $p^2 \leq 9$. In this case, each configuration with volume $32^3 \times 64$ takes around ~ 50 Gb storage, a huge number taking into account that GPU applications are usually not granted as much disk storage as CPU's. In the GPU clusters we run our code, we were granted between 5 and 20Tb of disk space, which we would fill with 100-400 configurations, a number that might hardly be enough for a single ensemble, let alone when dealing with several ensembles.

An obvious way to reduce storage needs is to transform the data from text to binary format, which will grant us a $\sim 70\%$ reduction in disk usage, although it will be still

a huge amount of data. A further reduction of storage requirements is only achieved through clever techniques; in our case we developed a binary-storage technique, inspired in the way the bits make up a byte. This technique reduced storage requirements up to $\sim 97\%$ without losing any relevant information.

	File.1	File.2	File.4	File.8
Weight:	1	2	4	8
Mask:	1	0	1	1
Total:	1	0	4	8

$= 13$

FIG. A.1: Example of construction of the inverse estimator using 13 sources in our storage method.

In order to understand the way the technique works, we can have a look at Fig. A.1. The byte is composed

of bits, and each bit has a different wait according to its position (1, 2, 4, ...). The idea is to mimic this structure for the stochastic sources. Since in the end we are going to average the sources, we can add several and store the addition in a single file; so in the file File.1 we store the contractions generated with one stochastic source, in File.2 we store the sum of the contractions coming from the second and the third stochastic source, and so on. Reconstruction is straightforward, taking into account the base-2 structure.

With this storage method one can recover the data for any number of sources, therefore we are keeping the same information in much less space. Actually some information is lost, for after storing the data there is only one way to recover a fixed number of sources, whereas before there could be many, but this extra information is not useful for us and can be discarded. In contrast, we gain a huge reduction in storage requirements, from $O(N)$ to $O(\log_2 N)$.

-
- [1] P. Boucaud et al. (ETM), Comput. Phys. Commun. **179**, 695 (2008), 0803.0224.
 - [2] C. Michael and C. Urbach (ETM Collaboration), PoS **LAT2007**, 122 (2007), 0709.4564.
 - [3] S. Dinter et al. (ETM Collaboration), JHEP **1208**, 037 (2012), 1202.1480.
 - [4] S. Bernardson, P. McCarty, and C. Thron, Comput. Phys. Commun. **78**, 256 (1993).
 - [5] J. Viehoff et al. (TXL Collaboration), Nucl. Phys. Proc. Suppl. **63**, 269 (1998), hep-lat/9710050.
 - [6] A. O'Cais, K. J. Juge, M. J. Peardon, S. M. Ryan, and J.-I. Skullerud (TrinLat Collaboration), pp. 844–849 (2004), hep-lat/0409069.
 - [7] J. Foley, K. Jimmy Juge, A. O'Cais, M. Peardon, S. M. Ryan, et al., Comput. Phys. Commun. **172**, 145 (2005), hep-lat/0505023.
 - [8] C. Alexandrou, K. Hadjiyiannakou, G. Koutsou, A. O'Cais, and A. Strelchenko, Comput. Phys. Commun. **183**, 1215 (2012), 1108.2473.
 - [9] S. Collins, G. Bali, and A. Schafer, PoS **LAT2007**, 141 (2007), 0709.3217.
 - [10] G. S. Bali, S. Collins, and A. Schafer, Comput. Phys. Commun. **181**, 1570 (2010), 0910.3970.
 - [11] C. McNeile and C. Michael (UKQCD Collaboration), Phys. Rev. **D63**, 114503 (2001), hep-lat/0010019.
 - [12] C. Alexandrou, M. Constantinou, S. Dinter, V. Drach, K. Jansen, et al. (2013), 1303.5979.
 - [13] K. Bitar, A. Kennedy, R. Horsley, S. Meyer, and P. Rossi, Nucl. Phys. **B313**, 377 (1989).
 - [14] S.-J. Dong and K.-F. Liu, Phys. Lett. **B328**, 130 (1994), hep-lat/9308015.
 - [15] T. Blum, T. Izubuchi, and E. Shintani (2012), 1208.4349.
 - [16] A. Stathopoulos and K. Orginos, SIAM J. Sci. Comput. **32**, 439 (2010), 0707.0131.
 - [17] A. Stathopoulos, A. Abdel-Rehim, and K. Orginos, J. Phys. Conf. Ser. **180**, 012073 (2009).
 - [18] C. Alexandrou, G. Koutsou, J. Negele, Y. Proestos, and A. Tsapalis, Phys. Rev. **D83**, 014501 (2011), 1011.3233.
 - [19] S. N. Syritsyn et al., Phys. Rev. **D81**, 034507 (2010), 0907.4194.
 - [20] C. Thron, S. Dong, K. Liu, and H. Ying, Phys. Rev. **D57**, 1642 (1998), hep-lat/9707001.
 - [21] R. Baron et al., JHEP **06**, 111 (2010), 1004.5284.
 - [22] M. Clark, R. Babich, K. Barros, R. Brower, and C. Rebbi, Comput. Phys. Commun. **181**, 1517 (2010), 0911.3191.
 - [23] R. Babich, M. Clark, B. Joo, G. Shi, R. Brower, et al. (2011), 1109.2935.
 - [24] L. Maiani, G. Martinelli, M. Paciello, and B. Taglienti, Nucl. Phys. **B293**, 420 (1987).
 - [25] S. Gusken (1999), hep-lat/9906034.
 - [26] S. Capitani, B. Knippschild, M. Della Morte, and H. Wittig, PoS **LATTICE2010**, 147 (2010), 1011.1358.
 - [27] C. Alexandrou, M. Constantinou, S. Dinter, V. Drach, K. Hadjiyiannakou, et al., PoS **LATTICE2012**, 163 (2012), 1211.4447.
 - [28] S. Dinter, V. Drach, and K. Jansen, PoS **QNP2012**, 102 (2012).
 - [29] S. Dinter, C. Alexandrou, M. Constantinou, V. Drach, K. Jansen, et al., Phys. Lett. **B704**, 89 (2011), 1108.1076.
 - [30] C. Alexandrou, M. Constantinou, S. Dinter, V. Drach, K. Jansen, et al., PoS **LATTICE2011**, 150 (2011), 1112.2931.
 - [31] J. Green, M. Engelhardt, S. Krieg, J. Negele, A. Pochinsky, et al. (2012), 1209.1687.
 - [32] J. Green, M. Engelhardt, S. Krieg, J. Negele, A. Pochinsky, et al., PoS **LATTICE2012**, 170 (2012), 1211.0253.
 - [33] S. Capitani, M. Della Morte, G. von Hippel, B. Jager, A. Jüttner, et al., Phys. Rev. **D86**, 074502 (2012), 1205.0180.
 - [34] A. Skouroupathis and H. Panagopoulos, Phys. Rev. **D79**, 094508 (2009), 0811.4264.
 - [35] C. Alexandrou et al., PoS **LATTICE2013**, 470 (2013).
 - [36] V. Azcoiti, E. Follana, A. Vaquero, and G. Di Carlo, JHEP **0908**, 008 (2009), 0905.0639.
 - [37] M. Clark, PoS **LAT2009**, 003 (2009), 0912.2268.
 - [38] <https://github.com/lattice/quda/tree/discLoop>